JOURNAL OF GEOPHYSICAL RESEARCH, VOL. 106, NO. B1, PAGES 553–566, JANUARY 10, 2001

Flow of variably fluidized granular masses across three-dimensional terrain 2. Numerical predictions and experimental tests

Roger P. Denlinger and Richard M. Iverson

U.S. Geological Survey, Vancouver, Washington

Abstract. Numerical solutions of the equations describing flow of variably fluidized Coulomb mixtures predict key features of dry granular avalanches and water-saturated debris flows measured in physical experiments. These features include time-dependent speeds, depths, and widths of flows as well as the geometry of resulting deposits. Three-dimensional (3-D) boundary surfaces strongly influence flow dynamics because transverse shearing and cross-stream momentum transport occur where topography obstructs or redirects motion. Consequent energy dissipation can cause local deceleration and deposition, even on steep slopes. Velocities of surge fronts and other discontinuities that develop as flows cross 3-D terrain are predicted accurately by using a Riemann solution algorithm. The algorithm employs a gravity wave speed that accounts for different intensities of lateral stress transfer in regions of extending and compressing flow and in regions with different degrees of fluidization. Field observations and experiments indicate that flows in which fluid plays a significant role typically have high-friction margins with weaker interiors partly fluidized by pore pressure. Interaction of the strong perimeter and weak interior produces relatively steep-sided, flat-topped deposits. To simulate these effects, we compute pore pressure distributions using an advection-diffusion model with enhanced diffusivity near flow margins. Although challenges remain in evaluating pore pressure distributions in diverse geophysical flows, Riemann solutions of the depth-averaged 3-D Coulomb mixture equations provide a powerful tool for interpreting and predicting flow behavior. They provide a means of modeling debris flows, rock avalanches, pyroclastic flows, and related phenomena without invoking and calibrating rheological parameters that have questionable physical significance.

1. Introduction

Three-dimensional (3-D) terrain can strongly influence the dynamics of rock avalanches, debris flows, and pyroclastic flows, but two difficulties have hindered development of flow dynamics models that include 3-D terrain effects. The first difficulty involves formulation of appropriate governing equations. *Iverson and Denlinger* [this issue] derive depth-averaged, frame-invariant governing equations that describe time-dependent flows of variably fluidized granular masses in which inertial forces, internal shear and normal forces, and boundary forces respond to 3-D boundary topography. The second difficulty, addressed in this paper, involves solving the governing equations and testing model predictions. We obtain stable, accurate numerical solutions of the hyperbolic, nonlinear governing equations by using a Riemann technique not previously applied to granular flow problems. We test numerical predictions against data from laboratory experiments in which parameter values, initial conditions, and boundary conditions are independently constrained. Comparisons with data indicate that the model predicts the behavior of both dry grain flows and water-saturated debris flows with considerable success.

Section 2 describes our numerical method for solving the variably fluidized grain flow equations of *Iverson and Denlinger* [this issue]. The method recasts the equations in terms of Riemann problems and employs a Harten-Lax-vanLeer-Contact (or HLLC) approximate Riemann solver [*Toro*, 1997] to generate solutions referenced to a fixed 3-D coordinate system. The Riemann method differs significantly from Lagrangian finite difference methods used in previous computations of dry granular avalanche motion [e.g., *Savage and Hutter*, 1989, 1991; *Greve et al*., 1994] and debris flow motion [*Iverson*, 1997a, 1997b]. Advantages of the Riemann formulation are greatest where multidimensional topographic influences are strongest [*Denlinger et al*., 1998]. For example, the Riemann formulation can address situations where flows on steep slopes encounter abrupt corners or constrictions or even divide and reunite as they pass around islands. The dynamics of such flows cannot be addressed in a satisfactory way by models that lack multidimensional momentum transport, no matter how complex a rheology is invoked [e.g., *Hungr*, 1995].

Section 3 describes two types of physical experiments that test our numerical predictions. One type of experiment, conducted using a miniature flume, involved flows of 290 cm^3 (0.00029 m^3) of dry, well-sorted sand. The sand discharged suddenly through gates of differing widths, then descended an inclined plane and stopped on a horizontal runout surface. Results of these experiments illustrate the conspicuous influence of 3-D path geometry on flow dynamics. The second type of experiment involved debris flows consisting of ~10 m^3 of poorly sorted, water-saturated sediment released at the U.S.

Paper number 2000JB900330.

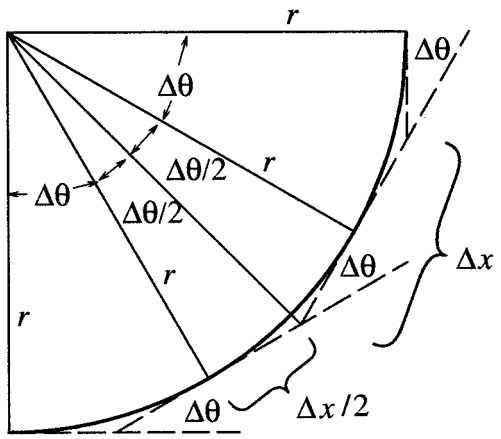

Figure 1. Schematic illustrating geometric relationships between a continuous radius of bed curvature r and the discrete units of cell length Δx and bed slope $\Delta\theta$ used in numerical calculations.

Geological Survey (USGS) debris flow flume [*Iverson et al.*, 1992]. Results of these experiments reveal the importance of interactions between nearly liquefied, fine-grained debris flow bodies and better drained, coarser-grained debris flow snouts.

2. Computational Methods

We describe our method for solving the depth-integrated equations of motion derived by *Iverson and Denlinger* [this issue], which we refer to here as the debris flow equations (DFE). These equations for conservation of mass and linear momentum are written in terms of a local, orthogonal Cartesian coordinate system in which the z coordinate is normal to each small (cell size) patch of ground. In general, this local coordinate system is rotated relative to the elevation, latitude, and longitude of the Earth's surface.

2.1. Governing Equations

In each local coordinate system (i.e., each cell or facet) the DFE may be divided by the mixture bulk density ρ and written in vector form as

$$\frac{\partial \mathbf{U}}{\partial t} + \frac{\partial \mathbf{F}}{\partial x} + \frac{\partial \mathbf{G}}{\partial y} = \mathbf{S}, \tag{1}$$

$$\mathbf{U} = \begin{bmatrix} h \\ h\bar{v}_x \\ h\bar{v}_y \end{bmatrix}, \tag{2}$$

$$\mathbf{F} = \begin{bmatrix} h\bar{v}_x \\ h\bar{v}_x^2 + \frac{1}{2}[(1-\lambda)k_{a/p} + \lambda]g_z h^2 \\ h\bar{v}_x\bar{v}_y \end{bmatrix}, \tag{3}$$

$$\mathbf{G} = \begin{bmatrix} h\bar{v}_y \\ h\bar{v}_y\bar{v}_x \\ h\bar{v}_y^2 + \frac{1}{2}[(1-\lambda)k_{a/p} + \lambda]g_z h^2 \end{bmatrix}, \tag{4}$$

$$\mathbf{S} = \begin{bmatrix} 0 \\ S_x \\ S_y \end{bmatrix}, \tag{5}$$

where

$$S_x = g_x h - \text{sgn}\,(\bar{v}_x)(1-\lambda)\left(g_z + \bar{v}_x^2 \frac{\partial \theta_x}{\partial x}\right) h \tan \varphi_{\text{bed}} - \frac{3\upsilon_f \mu}{\rho}\frac{\bar{v}_x}{h} + \frac{\upsilon_f \mu h}{\rho}\frac{\partial^2 \bar{v}_x}{\partial x^2} - \text{sgn}\left(\frac{\partial \bar{v}_x}{\partial y}\right) h k_{a/p} \cdot \frac{\partial}{\partial y}[g_z h(1-\lambda)] \sin \varphi_{\text{int}} + \frac{\upsilon_f \mu h}{\rho}\frac{\partial^2 \bar{v}_x}{\partial y^2}, \tag{6}$$

$$S_y = g_y h - \text{sgn}\,(\bar{v}_y)(1-\lambda)\left(g_z + \bar{v}_y^2 \frac{\partial \theta_y}{\partial y}\right) h \tan \varphi_{\text{bed}} - \frac{3\upsilon_f \mu}{\rho}\frac{\bar{v}_y}{h} + \frac{\upsilon_f \mu h}{\rho}\frac{\partial^2 \bar{v}_y}{\partial y^2} - \text{sgn}\left(\frac{\partial \bar{v}_y}{\partial x}\right) h k_{a/p} \cdot \frac{\partial}{\partial x}[g_z h(1-\lambda)] \sin \varphi_{\text{int}} + \frac{\upsilon_f \mu h}{\rho}\frac{\partial^2 \bar{v}_y}{\partial x^2}, \tag{7}$$

$$\lambda = \frac{p_{\text{bed}}}{\rho g_z h}, \tag{8}$$

$$k_{a/p} = k_{\text{act/pass}} = 2\,\frac{1 \mp [1 - \cos^2 \varphi_{\text{int}}(1 + \tan^2 \varphi_{\text{bed}})]^{1/2}}{\cos^2 \varphi_{\text{int}}} - 1. \tag{9}$$

In this set of equations, h is the flow depth normal to the local bed surface, $\bar{v}_x$ is the depth-averaged velocity in the x direction, $\bar{v}_y$ is the depth-averaged velocity in the y direction, g_x, g_y, and g_z are the components of gravitational acceleration in the x, y, and z directions, φ_{int} is the angle of internal friction of the granular solids, φ_{bed} is the friction angle of grains contacting the bed, υ_f is the fluid volume fraction (i.e., porosity), μ is the pore fluid viscosity, and λ is the ratio of the basal pore fluid pressure (p_{bed}) to the total basal normal stress. The lateral stress coefficient $k_{a/p}$ is derived by solving for the lateral thrust induced by the weight of a layer of Coulomb material that simultaneously slides along a rigid bed and yields internally [*Iverson*, 1997a]. Finally, θ_x and θ_y are the x and y components of the local bed slope (measured in radians from the horizontal).

In (6) and (7) the terms involving space derivatives of bed slope account for all effects of bed curvature (e.g., $\partial\theta_x/\partial x = 1/r_x$, where r_x is the x component of the local radius of curvature). These curvature terms represent the effects of coordinate transformations that show how changes in bed slope redirect x and y momentum components to keep them parallel to the bed [e.g., *Savage and Hutter*, 1991]. Redirection of the x and y momentum components influences basal normal stresses and thereby produces changes in basal frictional resistance and flow thickness [*Iverson and Denlinger*, this issue]. Where finite changes in bed slope occur between adjacent computational cells, we use the approximation $\partial\theta_x/\partial x \approx \tan(\Delta\theta_x/2)/(\Delta x/2)$ to account for bed curvature (Figure 1).

2.2. Riemann Formulation

To solve the DFE using a Riemann method, we compute the speeds and directions of elementary waves that determine fluxes of the conserved variables **U** by propagating information about **U** in space and time [e.g., *Toro*, 1997]. To characterize these mathematical waves, we first use the chain rule to rewrite the DFE in terms of Jacobian matrices **A** and **B** of the flux vectors **F**(**U**) and **G**(**U**). Then (1) becomes

$$\frac{\partial \mathbf{U}}{\partial t} + \mathbf{A} \cdot \frac{\partial \mathbf{U}}{\partial x} + \mathbf{B} \cdot \frac{\partial \mathbf{U}}{\partial y} = \mathbf{S}, \tag{10}$$

where

$$\mathbf{A} = \frac{\partial \mathbf{F}}{\partial \mathbf{U}} = \begin{bmatrix} 0 & 1 & 0 \\ c^2 - \bar{v}_x^2 & 2\bar{v}_x & 0 \\ -\bar{v}_x\bar{v}_y & \bar{v}_y & \bar{v}_x \end{bmatrix}, \tag{11a}$$

$$\mathbf{B} = \frac{\partial \mathbf{G}}{\partial \mathbf{U}} = \begin{bmatrix} 0 & 0 & 1 \\ -\bar{v}_x\bar{v}_y & \bar{v}_y & \bar{v}_x \\ c^2 - \bar{v}_y^2 & 0 & 2\bar{v}_y \end{bmatrix}, \tag{11b}$$

and c is the speed of ideal gravity waves given by

$$c = \sqrt{[(1 - \lambda)k_{a/p} + \lambda]g_z h}. \tag{12}$$

This definition of the gravity wave speed c fundamentally distinguishes the DFE from standard shallow-water equations like those analyzed by *Vreugdenhil* [1994]. As defined in (12), c includes the effects of Coulomb friction and denotes the maximum rate of information propagation due to lateral stress transfer in the grain-fluid mixture. Consequently, (12) implies that regions of compressing flow (with generally large values of $k_{a/p}$) propagate information faster than regions of extending flow (with generally small values of $k_{a/p}$). For the special case of a completely liquefied Coulomb mixture ($\lambda = 1$), the gravity wave speed defined by (12) reduces to the standard shallow-water expression and lacks dependence on compression and extension of the flow.

The Jacobian matrices **A** and **B** defined in (11) have real eigenvalues, making the DFE fully hyperbolic. The matrices are singular when the speed of the flow equals the gravity wave speed c, in which case the flow is critical. (Despite enormous dissipative effects of Coulomb friction, critical flow is common in debris flows and avalanches because flows <10 m thick commonly occur on steep slopes and achieve speeds >10 m/s.) A straightforward analysis yields the following eigenvalues for **A** and **B**, which describe the local speeds of waves in the x and y directions:

$$\mathbf{A}: \begin{array}{l} a(1) = \bar{v}_x + c \\ a(2) = \bar{v}_x \\ a(3) = \bar{v}_x - c \end{array} \qquad \mathbf{B}: \begin{array}{l} b(1) = \bar{v}_y + c \\ b(2) = \bar{v}_y \\ b(3) = \bar{v}_y - c \end{array} \tag{13}$$

The local directions of waves with simultaneous x and y components are given by the corresponding eigenvectors of a diagonalizable composite matrix **Q**, where $\mathbf{Q} = \mathbf{A}n_x + \mathbf{B}n_y$ and n_x and n_y are the components of any unit vector **n** in the x-y plane [*Toro*, 1997]. The right and left eigenvector matrices are the same as those for shallow-water equations (with a different definition of the gravity wave speed c, as specified by (12)) and are given by *Alcrudo and Garcia-Navarro* [1993, equation 9]. Together these eigenvectors and eigenvalues provide the information needed to propagate fluxes of mass and momentum in the correct direction at the correct speed.

2.3. Numerical Integration

Once the wave directions and speeds are known, we integrate the DFE numerically using two-step, finite volume procedure. In the first step an intermediate solution is obtained by solving the homogeneous part of (1). Thus we temporarily set $\mathbf{S} = 0$, then integrate (1) over a finite control volume V and apply Gauss' theorem to convert volume integrals to surface integrals, yielding

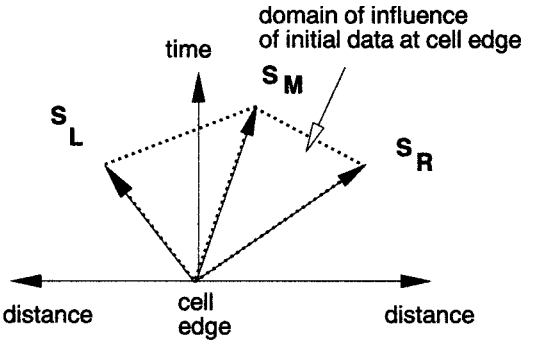

Figure 2. Schematic of the border between neighboring computational cells, illustrating time and space coordinates and waves that govern fluxes across cell edges.

$$\int_V \frac{\partial \mathbf{U}}{\partial t}\, dV + \int_A (\mathbf{F}_c \cdot \mathbf{n})\, dA + \int_A (\mathbf{G}_c \cdot \mathbf{n})\, dA = 0. \tag{14}$$

Here the volume integral uses the average **U** within each computational cell, although **U** may vary nonlinearly within any cell. The area integrals sum the composite Riemann fluxes $\mathbf{F}_c$ and $\mathbf{G}_c$ normal to the surfaces that form cell walls. In general, cells may have any number of sides, but here we use quadrilateral cells on a regular grid aligned with the x and y coordinates. The discussion below focuses on the x component of the Riemann flux ($\mathbf{F}_c$) in a multidimensional flow field, but analogous equations apply to the y component ($\mathbf{G}_c$).

We use the HLLC approximate Riemann solver to calculate Riemann fluxes across each cell wall as described by *Toro* [1997, chapter 10]. (The Riemann flux is the contribution from each cell wall to the cell-averaged flow vector during the time interval dt.) The evolution of the cell-averaged flow vector may be written in terms of waves (Figure 2). Three wave speeds are needed. The speeds S_R and S_L bound the wave field across the cell wall for the time interval dt and define the domain of influence of initial variables at cell walls. The speed S_M determines whether momentum fluxes across cell walls are directed from the right or the left. By applying the integral form of the conservation laws (14) over appropriate control volumes, *Toro* [1997, chapter 10] obtains the HLLC numerical approximation of the composite Riemann flux on a cell wall,

$$\mathbf{F}_c|_{i+1/2} = \begin{cases} \mathbf{F}_L, & 0 \le S_L \\ \mathbf{F}_{LM}, & S_L \le 0 \le S_M \\ \mathbf{F}_{RM}, & S_M \le 0 \le S_R \\ \mathbf{F}_R, & 0 \ge S_R \end{cases} \tag{15}$$

where

$$\mathbf{F}_L = \mathbf{F}(\mathbf{U}_i), \tag{16a}$$

$$\mathbf{F}_{LM} = \mathbf{F}_L + S_L(\mathbf{U}_{LM} - \mathbf{U}_L), \tag{16b}$$

$$\mathbf{F}_{RM} = \mathbf{F}_R + S_R(\mathbf{U}_R - \mathbf{U}_{RM}), \tag{16c}$$

$$\mathbf{F}_R = \mathbf{F}(\mathbf{U}_{i+1}), \tag{16d}$$

$$\mathbf{U}_L = \mathbf{U}_i, \tag{16e}$$

$$\mathbf{U}_R = \mathbf{U}_{i+1}, \tag{16f}$$

$$\mathbf{U}_{LM} = h_L \frac{S_L - \bar{v}_x|_L}{S_L - S_M} \begin{bmatrix} 1 \\ S_M \\ \bar{v}_y|_L \end{bmatrix}, \tag{16g}$$

$$\mathbf{U}_{RM} = h_R \frac{S_R - \bar{v}_x|_R}{S_R - S_M} \begin{bmatrix} 1 \\ S_M \\ \bar{v}_y|_R \end{bmatrix}. \tag{16h}$$

Here i is a spatial index, which indicates that $\mathbf{F_c}|_{i+1/2}$ represents the flux normal to the boundary separating cells i and $i + 1$. Subscripts R and L designate quantities on the right and left sides of a cell wall.

To calculate the wave speeds S_L, we first define the quantities

$$q_L = \begin{cases} \left[\dfrac{(\Phi_L + \Phi_M)\Phi_M}{2\Phi_L^2}\right]^{1/2}, & \Phi_L < \Phi_M, \\ 1, & \Phi_L \geq \Phi_M, \end{cases} \tag{17a}$$

$$q_R = \begin{cases} \left[\dfrac{(\Phi_R + \Phi_M)\Phi_M}{2\Phi_R^2}\right]^{1/2}, & \Phi_R < \Phi_M, \\ 1, & \Phi_R \geq \Phi_M, \end{cases} \tag{17b}$$

$$\Phi_L = \tfrac{1}{2}\,(k_{a/p}|_L + k_{a/p}|_R)(1 - \lambda_L)\, g_z h_L, \tag{18a}$$

$$\Phi_R = \tfrac{1}{2}\,(k_{a/p}|_L + k_{a/p}|_R)(1 - \lambda_R)\, g_z h_R, \tag{18b}$$

$$\Phi_M = [\tfrac{1}{2}\,(c_L + c_R) + \tfrac{1}{4}\,(\bar{v}_x|_L - \bar{v}_x|_R)]^2. \tag{18c}$$

In these equations, subscripts R and L refer to right- and left-going waves emanating from a cell boundary and M refers to the middle region (in space-time) between these waves (Figure 2). For nonzero values of Φ_R and Φ_L (i.e., for nonzero flow depths to the left and right of the cell) the wave speeds are given by [*Toro*, 1997]

$$S_R = \bar{v}_x|_R - c_R q_R, \tag{19a}$$

$$S_M = \tfrac{1}{2}\,(\bar{v}_x|_L + \bar{v}_x|_R) + c_L - c_R, \tag{19b}$$

$$S_L = \bar{v}_x|_L - c_L q_L. \tag{19c}$$

These speeds govern the composite Riemann flux at the edges of most computational cells. Exceptions occur at the front of a propagating surge or the tail of a receding flow. We consider such situations in section 2.4.

The second step of the numerical integration accounts for the effect of the nonzero source term $\mathbf{S}$ by substituting the intermediate solution for $\mathbf{U}$ obtained from the HLLC Riemann solver into the ordinary differential equation

$$d\mathbf{U}/dt = \mathbf{S}. \tag{20}$$

We integrate (20) using an explicit Euler method that gives first-order accuracy for spatial and temporal gradients in the flow [*Harten et al*., 1983; *Toro*, 1997, chapter 10]. We tested the convergence of the method by computing solutions using four different cell sizes, in each case halving the cell size. The solutions we report here are for the largest cells that produced no change in results with continued cell size reduction. Limits on the maximum size of time steps Δt in these integrations are identified by a von Neumann stability analysis [*Toro*, 1997, p. 163], which indicates that the Courant-Fredrichs-Lewy number (defined here as CFL = $[(\bar{v}_x^2 + \bar{v}_y^2)^{1/2} + c]\Delta t/\Delta x$, where Δx is the minimum grid cell size) must be less than or equal to one to ensure numerical stability. Accordingly, in our computations with a fixed grid we alter the time step size as flow proceeds and values of c, $\bar{v}_x$, and $\bar{v}_y$ evolve. At any time we identify the maximum value of $[(\bar{v}_x^2 + \bar{v}_y^2)^{1/2} + c]$ within the flow domain, and with this value adjust Δt so that CFL = 0.8 for the next time step. This methodology yields first-order solutions that are economical and suitably accurate, as we demonstrate by tests against experimental data described below.

2.4. Flow Front Propagation

Advancing or receding flow fronts occur wherever zero flow depth exists adjacent to a cell. Our means of computing the speeds of such fronts follows a rationale like that of *Toro* [1997, p. 140] for an analogous problem involving vacuum fronts in shock tubes. Here we focus on the equation governing the speed of a flow front advancing in the right-hand (positive x) direction, but analogous equations apply to advancing and receding fronts in all directions.

A fundamental difficulty results from lack of definable wave speeds in advance of a flow front. Owing to the ambient condition $h = 0$, S_R and S_M as defined in (19a) and (19b) do not exist in advance of a flow front, and right-hand Riemann fluxes cannot be calculated. However, the left-going wave emanating from the flow front (with speed given by S_L in (19c)) contains information that constrains the front speed. Mass and momentum conservation dictate that this wave propagates in a manner that preserves a quantity (known as a Riemann invariant) defined by

$$I_L = \bar{v}_x|_L + 2c_L \tag{21}$$

for the case $S_x = 0$. Moreover, near the flow front (where $h \to 0$ and $v_f \to 0$) it is reasonable to assume that $S_x \to 0$, and we therefore assume that I_L is approximated well by (21). We then equate values of I_L at the flow front (denoted by subscript zero) and at any other point just upstream of the flow front, yielding

$$\bar{v}_x|_0 + 2c_0 = \bar{v}_x|_L + 2c_L. \tag{22}$$

However, near the flow front the gravity wave speed c approaches zero because $h \to 0$, and precisely at the front, $c_0 = 0$ exactly. Substituting this value in (22) and combining the result with (21) yields

$$\bar{v}_x|_0 = I_L, \tag{23}$$

which indicates that the speed of the mixture at the flow front equals the Riemann invariant associated with the left-going rarefaction wave emanating from the flow front. Moreover, since the mixture thickness tapers to zero at the flow front, the mixture speed equals the speed of the front itself. Effectively, the speed of the right-going front is dictated by the rate at which material discharges from the left.

2.5. Basal Pore Pressure Distributions

The depth-averaged DFE include no variations in any quantity through the flow thickness: a simplification that presents challenges for simulating the influence of evolving pore fluid pressures. Such evolution is important in geophysical flows where fluid forces may play a significant role. *Iverson and Denlinger* [this issue] describe a model in which pore pressure simultaneously advects downstream with the flowing debris and diffuses normal to the bed. Only the computed basal pore

Table 1. Material Properties and Dimensionless Parameters for Physical Experiments and Model Predictions[a]

Property or Parameter	Granular Avalanche Experiments	Debris Flow Experiments
Basal friction angle φ_{bed}, deg	29 ± 1.4	28 ± 0.7
Internal friction angle φ_{int} deg	40 ± 1.0	42 ± 0.4
Solid volume fraction v_s	0.6 (loose static state)	0.6 (static and dynamic states)
Fluid volume fraction v_f	0.4 (loose static state)	0.4 (static and dynamic states)
Fluid viscosity μ, Pa s	2×10^{-5} (air)	0.1 (muddy water)
Solid density ρ_s, kg/m^3	2650 (quartz)	2700 (quartz, feldspar, etc.)
Fluid density ρ_f, kg/m^3	1 (air)	1200 (muddy water)
Mixture bulk density ρ, kg/m^3	1600	2000
Typical grain diameter δ, m	0.0005 (medium sand)	0.01 (gravel)
Hydraulic permeability k, m^2	10^{-11} (estimated for loose sand)	10^{-11} (permeameter tests)
Hydraulic diffusivity D, m^2/s	0.05 (estimated for loose sand)	10^{-4} (consolidation tests)
Initial pore pressure ratio κ	0	0.9
Average shear rate $\dot{\gamma}$, s^{-1}	~50 (mean velocity ÷ H)	~50 (mean velocity ÷ H)
Maximum flow thickness H, m	0.01	0.2
Maximum flow length L, m	0.5	100
Aspect ratio ε	0.02	0.002
Savage number N_S	0.006	0.2
Bagnold number N_B	7000	600
Fluidization number N_f	0.009	7×10^{-8}
Quasi-Reynolds number N_R	5×10^6	3×10^5
Pore pressure number N_p	100	0.008

[a]Friction angle data include means and standard deviations computed from 10 to 15 tipping table measurements with each type of material. For other parameters we list appropriate average values taken from *Iverson* [1997a], *Iverson et al*. [1997], *Major et al*. [1997], and *Freeze and Cherry* [1979]. To compute Bagnold numbers, maximum solid volume fractions were assumed equal to 0.7 [cf. *Iverson and Denlinger*, this issue].

pressure (indicated by λ) enters depth-averaged calculations of flow dynamics. Here, in our numerical simulations of water-saturated debris flows we employ the advective diffusion model and assume that pore pressures are hydrostatic until the debris begins to move. When movement commences, we specify that pore pressures rise linearly over the course of 1 s to a value $\lambda = 0.9$ and then begin to decay diffusively as they advect downstream. This behavior mimics behavior measured in debris flow initiation experiments [*Iverson et al*., 1997; *Reid et al*., 1997].

In addition to our formulation for pore pressure advection and diffusion we employ a kinematic criterion to identify regions of enhanced pore pressure depletion near flow fronts. Experiments and field observations indicate that grain size segregation causes accumulation of coarse clasts and low pore pressures near fronts of debris flow surges [*Iverson*, 1997a]. To simulate this behavior, we assume that a coarse-grained front with high pore pressure diffusivity is present wherever one or more the following kinematic conditions are satisfied:

$$\bar{v}_x > 0, \qquad \partial h/\partial x < 0, \tag{24a}$$

$$\bar{v}_x < 0, \qquad \partial h/\partial x > 0, \tag{24b}$$

$$\bar{v}_y > 0, \qquad \partial h/\partial y < 0, \tag{24c}$$

$$\bar{v}_y < 0, \qquad \partial h/\partial y > 0. \tag{24d}$$

These criteria indicate that flow thickness diminishes in the downstream direction. (To minimize the influence of numerical fluctuations in computations, we use a threshold value 0.001 to approximate zero thresholds for $|\partial h/\partial x|$ and $|\partial h/\partial y|$ in (24a)–(24d).) This simplistic treatment of the effects of grain size sorting on flow front dynamics represents a rough approximation of the processes in nature; it causes dissipation of flow front pore pressures commensurate with data and observations, and it can be implemented in a depth-averaged model. More sophisticated analyses of grain size segregation, pore pressure dissipation, and flow front dynamics could be achieved by developing three-dimensional models without depth averaging.

3. Experimental Methods

To test our numerical predictions, we use data from small-scale experiments with flows of dry sand and large-scale experiments with flows of water-saturated sand and gravel. Table 1 lists five dynamic scaling parameters that must be considered in designing and interpreting such experiments [*Iverson and Denlinger*, this issue]. Three of these scaling parameters, the Savage number N_S, Bagnold number N_B, and fluidization number N_f, reflect grain-scale processes and indicate whether Coulomb mixture theory provides an adequate description of a particular grain-fluid flow. The other two scaling parameters, N_R and N_p, reflect continuum-scale processes in flows that are described adequately by depth-averaged Coulomb mixture theory.

Values of N_R and N_p guide design and interpretation of experiments with Coulomb mixtures by characterizing the degree to which fluid stresses influence the behavior of the mixture as a whole. The parameter N_R is similar to a conventional Reynolds number but differs in that it describes the characteristic ratio of inertial stresses in the mixture to viscous stresses in the fluid phase alone. The parameter N_p describes the tendency for persistence of high pore fluid pressures that reduce intergranular stresses and transfer stresses to the fluid phase. Values of N_R or N_p of order 1 or smaller indicate that pore fluid viscosity or pressure may play a key role in flow dynamics. Values of N_R and N_p much greater than 1 indicate negligible importance of fluid viscosity and pressure and denote dry granular avalanche behavior like that investigated by *Savage and Hutter* [1989, 1991], *Greve et al*. [1994], and *Wieland et al*. [1999].

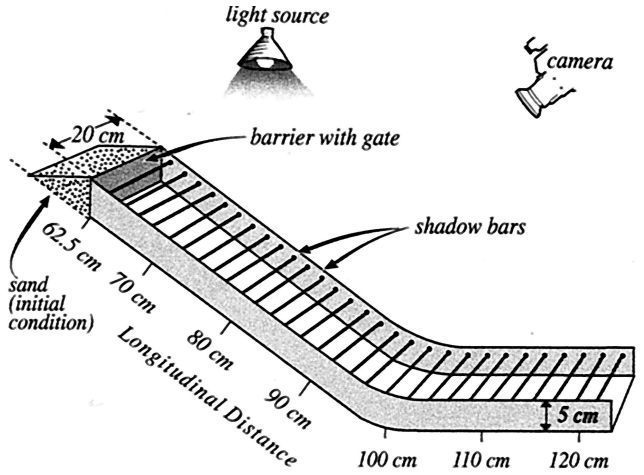

Figure 3. Schematic of the miniature flume used to conduct dry sand flow experiments. Distances between light source, camera, and flume are ~2 m and are not shown to scale.

For cases in which fluid effects are negligible, experiments with dry granular avalanches can be conducted at any convenient scale because the depth-averaged Coulomb mixture theory reduces to a form that uses only the friction angles (φ_{bed}, φ_{int}) and system geometry as input. Of course, the scale of granular avalanche experiments must be large enough to satisfy the continuum assumption and to minimize the effects of microscopic forces (such as those due to electrostatic charges) that are not considered in the theory but which might influence macroscopic mechanics.

For cases in which pore fluid effects are significant, great care must be taken in designing and interpreting experiments intended to simulate large-scale geophysical flows. Commonly, geophysical flows have large values of N_R but small values of N_p, indicating that viscous stresses are negligible but pore pressure effects are not [*Iverson and Denlinger*, this issue]. Such conditions can be impossible to achieve in miniature experiments with sediment-water mixtures because N_R decreases but N_p increases as flow size decreases. Indeed, miniature flows of sediment-water mixtures might exhibit significant viscous effects but little pore pressure effect, exactly the opposite of most large-scale geophysical flows. Miniature flows may also exhibit effects due to surface tension at air-water interfaces. Better similitude can be achieved by conducting experiments with sediment-water mixtures at scales large enough to approximate geophysical conditions.

3.1. Small-Scale Granular Avalanche Experiments

Our granular avalanche experiments employed a rectangular flume with a bed surface inclined 31.4° adjoined to a horizontal runout surface by a curved section with a 10-cm radius of curvature (Figure 3). In each experiment, 290 cm^3 of loosely packed, well-sorted, well-rounded dry quartz sand with grain diameters ~0.5 mm was placed behind a vertical wall positioned 37.5 cm upslope from the break in slope. The sand was graded to produce a level surface, then discharged suddenly by opening a spring-loaded gate. In one type of experiment the gate spanned the entire flume width (20 cm), and in a second type it spanned a slot 4 cm wide in the center of the flume. The narrow gate caused marked convergence and divergence of flow as sand passed through the gate, which revealed the importance of multidimensional momentum transport and internal shearing on planes normal to the flume bed.

In each dry sand experiment the flume bed was surfaced with Formica that had a consistent, hard, moderately smooth finish and little tendency to adsorb water vapor or hold electrostatic charges. Vertical sidewalls of the flume were constructed of painted aluminum and clear polycarbonate. Table 1 summarizes values of static bed friction angles and internal friction angles measured using tipping-table tests of sand sliding across the Formica, painted aluminum, and polycarbonate surfaces and of sand shearing internally. Table 1 also lists values of other pertinent sand properties and values of N_S, N_B, N_f, N_R, and N_p calculated for these experiments. Large values of N_R and N_p indicate that fluid stresses were negligible and that the small-scale experiments were appropriate for investigating motion of dry granular avalanches.

Several replicates of each sand flow experiment were recorded on time-stamped videotapes and still-frame photographs. Examination of videotapes and photographs indicated that the timing and extent of sand flow were nearly identical in replicate experiments and that differences were not resolvable using our measurement techniques. Therefore we present data from only one experiment of each type.

A noninvasive optical shadowing technique was used to measure sand thicknesses during and after flow. To produce shadows, each experiment was illuminated directionally by a 1000-W halogen lamp that cast light obliquely on the flume bed. Filming and videotaping were performed from a different oblique angle (Figure 3). Shadowing rods 1.5 mm in diameter were positioned horizontally 2–3 cm above the flume bed so that they spanned the width of the flume at 2-cm intervals along the flume's length. As viewed on videotapes and photographs, shadows cast by the rods upon the underlying sand were offset by differing distances depending on the sand thickness. Calibrations that related observed shadow offsets to sand thicknesses along the length of the flume were obtained by placing static objects of known thickness under the shadow bars and measuring the resulting offset. These empirical calibrations eliminated the need to consider complex optical effects that could bias interpretation of shadow offsets.

In each experiment, sand thicknesses normal to the flume bed were inferred from shadow offsets measured on digitized 35-mm photographs taken at intervals ~0.2 s with shutter speeds of 1/1000 s. Photographs provided better optical resolution than freeze-frame video images, but correlation with videotapes was used to establish the timing of photographs due to the superior video time stamp resolution (0.01 s). Shadow offsets were measured along the shadow lines at 1-cm intervals or at smaller intervals where sharp gradients in sand thickness occurred. Inferred sand thicknesses were then contoured using commercial software. Comparison of contoured sand thicknesses with direct measurements of sand thicknesses in static deposits indicated that errors due to shadow measurements and contouring were generally <1 mm.

3.2. Large-Scale Debris Flow Experiments

Experiments with debris flows of ~10 m^3 of water-saturated sand and gravel (containing <2% silt and clay by weight) were conducted at the USGS debris flow flume, a rectangular concrete chute 95 m long and 2 m wide that slopes 31° throughout most of its length and flattens at its base to adjoin an unconfined runout surface that slopes $2\frac{1}{2}°$ (Figure 4). Details of the flume facility and experimental methods have been reported

elsewhere [*Iverson et al*., 1992; *Iverson and LaHusen*, 1993; *Iverson*, 1997a; *Major and Iverson*, 1999]. Here we report results of two experiments that differed only in the distance of flow confinement by rigid channel walls. In one experiment (April 19, 1994) the flow was unconfined as it crossed the runout surface. In the other experiment (July 24, 1995) the flow was confined by concrete panels that effectively extended the flume length 7.4 m across the runout surface. Differing distances of confinement revealed the effects of flow front friction and lateral spreading on debris flow dynamics and deposition.

The mechanics of debris flows are more complex those that of dry granular avalanches owing to the presence of a relatively viscous, dense fluid phase composed of water and suspended fine sediment [*Iverson*, 1997a]. Values of the dimensionless parameters N_S, N_B, N_f, N_R, and N_p indicate that our flume debris flows behave as Coulomb mixtures in which viscous stresses are small but pore fluid pressures are significant (Table 1).

With one exception, independent measurements established the values of all material properties in our experiments (Table 1) [cf. *Iverson*, 1997a; *Iverson et al*., 1997; *Major et al*., 1997]. The exception arose from sorting and selective transport of large clasts, which produced accumulations of coarse sediment at debris flow snouts that consequently sustained little or no positive pore fluid pressure [*Iverson*, 1997a, 1997b; *Major and Iverson*, 1999]. We were unable to measure the hydraulic diffusivity of these coarse-grained snouts owing to their very rapid loss of pressure, but the diffusivity clearly exceeded the value $D = 10^{-4}$ m^2/s measured for our unsorted debris flow slurries. For testing model predictions we assigned coarse-grained snouts a hydraulic diffusivity $D = 10^{-2}$ m^2/s. This value causes pore pressure depletion within a few seconds in flows ~0.1 m thick, consistent with qualitative observations.

In each experiment, measurements of flow depths and speeds and deposit locations and geometries tested model predictions of debris flow behavior. Laser and ultrasonic ranging devices measured flow depths at high frequencies (20–1000 Hz) as debris flows passed instrumented cross sections 2 m, 33 m, and 67 m downslope from the gate at the flume head. The same measurements constrained flow speeds by indicating travel times between the gate and the three instrumented cross sections. Additional measurements of flow speed between cross sections and in the runout area were obtained from time-stamped videotapes synchronized with the data acquisition system. Photographs, videotapes, and topographic surveys of ~100 points established the position and geometry of debris flow deposits. Topographic surveys yielded isopach maps that provide quantitative comparisons with model predictions of runout distances and deposit geometries.

4. Results

Figures 5–9 illustrate comparisons between computational and experimental results. These comparisons help evaluate the most important aspects of model performance. For small-scale experiments with dry sand we compare isopach maps that show distributions of sand thickness (measured normal to the bed) before, during, and after each flow. Computations to predict the results of these experiments used square grid cells 0.25 cm^2 (0.000025 m^2) in size, yielding roughly 6000 cells for the flow domain. For large-scale experiments with water-saturated debris we compare depth-time graphs for flow along the flume centerline at three cross sections, and we compare isopach maps of deposit geometries as well as qualitative observations of deposit liquefaction. Computations to predict the results of these experiments used square grid cells 0.0625 m^2 in size, yielding roughly 6000 cells for the flow domain.

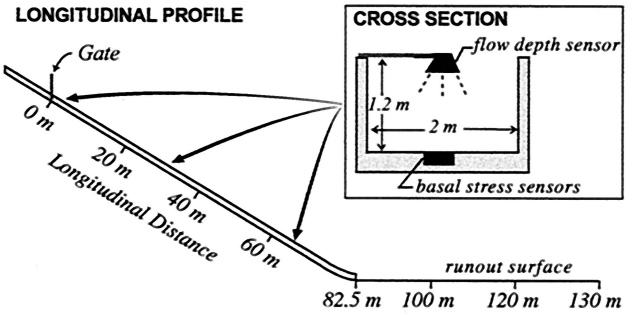

Figure 4. Schematic of the U.S. Geological Survey (USGS) debris flow flume, used to conduct experiments with water-saturated sand-gravel mixtures.

4.1. Dry Sand Flows

Figure 5 depicts results for the dry sand flow released suddenly from behind a vertical gate that spanned the flume width. The flow accelerated, elongated, and thinned rapidly after the gate opened. When the leading edge of the flow reached the break in slope 37.5 cm downslope from the gate, only a small percentage of the sand was still evacuating the area upslope from the gate. Sand that first reached the depositional area was pushed forward only slightly by subsequently arriving sand, and deposition was complete 1.5 s after flow release. Videotape recordings indicate that motion of the sand involved a combination of basal sliding and internal deformation. Effects of flume sidewall friction appeared slight except in the source area behind the gate. Sand adjacent to sidewalls evacuated the area behind the gate somewhat more slowly than did sand closer to the flume centerline, and sand along the sidewalls was the last to be deposited. However, this sidewall effect and multidimensional momentum transport appeared to have little effect on flow and deposition.

Figure 5 indicates that predictions of the numerical model fit the observed timing and depth of sand flow and the geometry of the resulting deposit quite well. Model predictions of the timing and total travel distance of the flow front and of the final deposit geometry are particularly accurate. Predictive errors involve mostly the details of individual isopach shapes and locations, which are irregular in the experimental results but smooth in the model predictions.

Figure 6 illustrates results for conditions similar to those depicted in Figure 5 but with the 20-cm-wide gate replaced by the 4-cm-wide gate. The narrow gate impeded sand discharge and caused pronounced cross-slope momentum transport as the flow converged and then diverged while passing through the gate opening. Frictional energy dissipation associated with this convergence and divergence caused the flow to move as a slower, thinner sheet than in the wide-gate experiment (compare Figure 5). Completion of deposition required ~5 s with the narrow gate, in contrast to 1.5 s required with the wide gate. With both gates, deposition was focused at the break in slope at the 100-cm mark shown in Figures 5 and 6. However, discharge through the narrow gate produced a deposit with an upward tapering wedge shape, in contrast to the more blunt

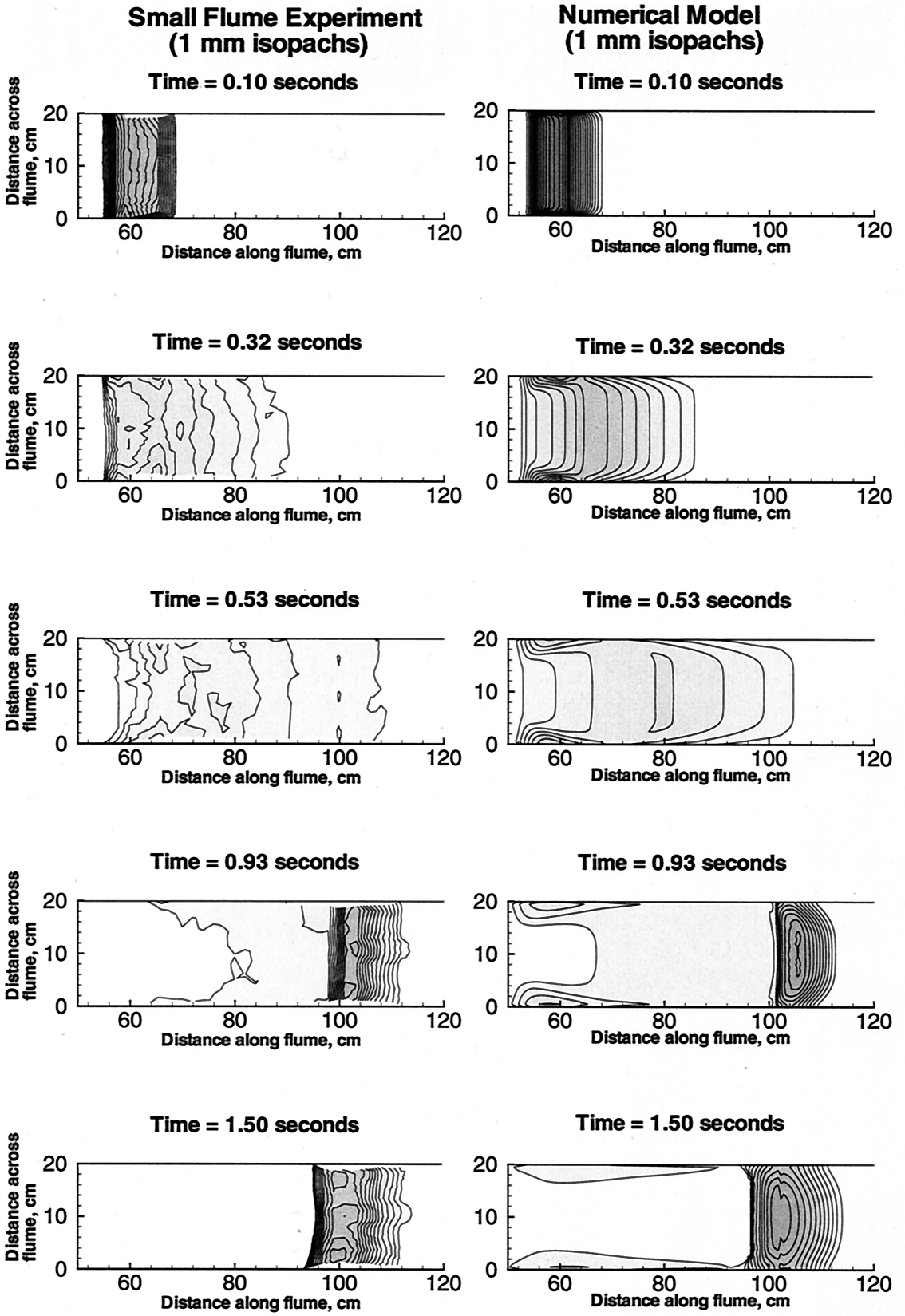

Figure 5. Maps comparing experimental data and model predictions for flow of dry sand released instantaneously from behind a wide (20 cm) gate in the small flume (Figure 3). The gate opened at time zero. Contours depict 1-mm isopachs of sand thickness normal to the bed.

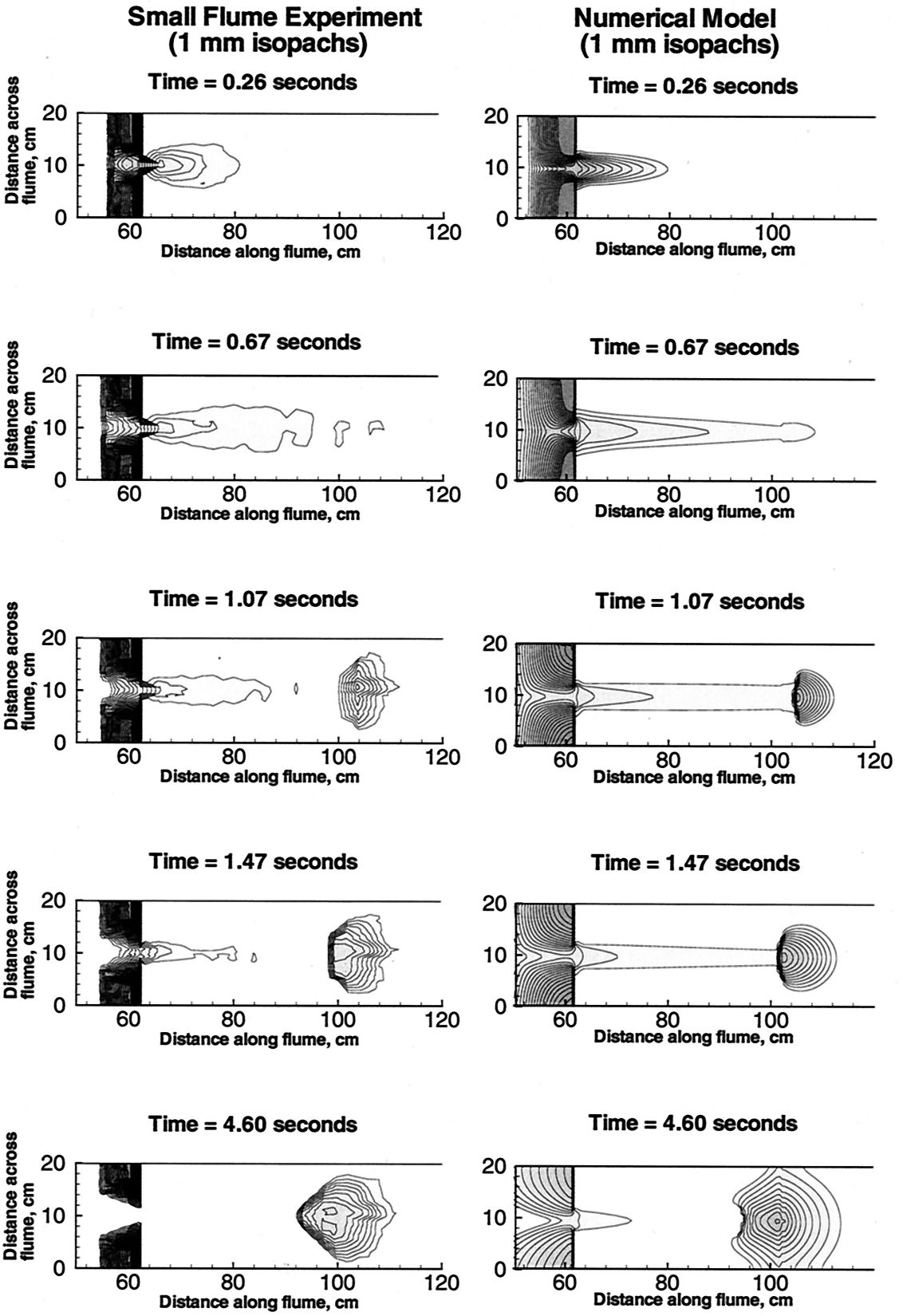

Figure 6. Maps comparing experimental data and model predictions for flow of dry sand released instantaneously from behind a narrow (4 cm) gate in the small flume (Figure 3). The gate opened at time zero. Contours depict 1-mm isopachs of sand thickness normal to the bed.

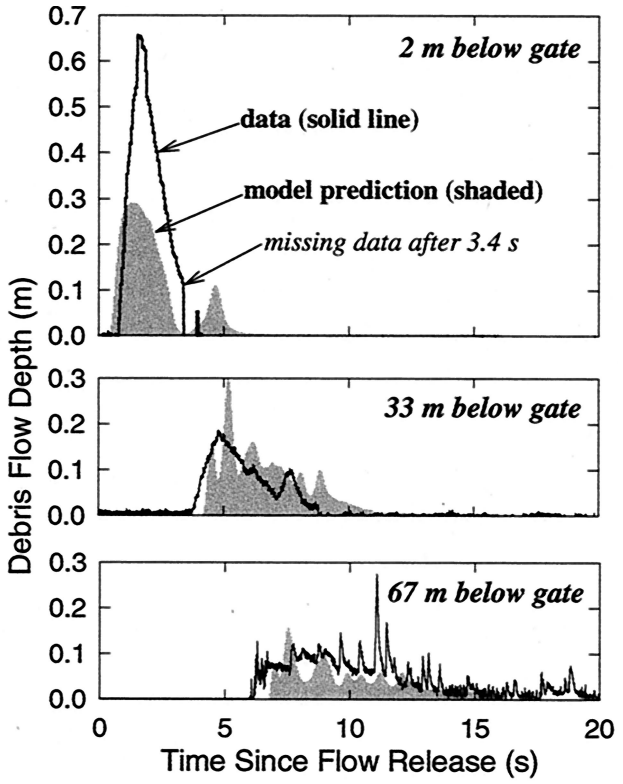

Figure 7. Comparison of measurements and model predictions of flow depths at three cross sections in a water-saturated debris flow at the USGS flume, April 21, 1994. Downslope distance is measured from the base of the gate at the flume head, and time is measured from the instant the gate opens.

deposit produced with the wide gate. The wedge shape resulted from sediment accumulation during the last stages of discharge through the narrow gate. More importantly, the narrow gate left a considerable mass of static sand stranded in pyramid-like heaps against the upslope side of the barrier at 62.5 cm (Figure 6). This sand was restrained by Coulomb friction that resisted shear transverse to the flume slope. Analogous resistance does not occur in one-dimensional flows of granular solids or in flows of liquids without yield strength.

Figure 6 indicates that model predictions compare well with results of the narrow-gate experiments. Flow timing, depth, and depositional pattern all match approximately. The largest discrepancies between model predictions and data occur as a result of very thin flow (~1 grain diameter thick), where the Coulomb continuum model is inappropriate. For example, much of the upward tapering margin of the measured deposit resulted from accumulation of saltating grains, which are not simulated by the model. Despite such discrepancies the final deposit shape and time of deposition shown in Figure 6 exhibit relatively small errors. Model predictions for the narrow gate leave sand stranded behind the vertical barrier at 62.5 cm, just as measured in experiments. However, the model predicts that the heap of sand behind the gate undergoes smoothing and stretching due to numerical creep that results from imperfect balancing of static driving and resisting forces. The same numerical creep allows a trickle of sand to escape from behind the barrier even after deposition has effectively ceased, but this shortcoming has little effect on the final deposit geometry.

4.2. Water-Saturated Debris Flows

Figures 7–9 compare model predictions with data from large-scale debris flow experiments. Figures 7 and 8 compare computed stage hydrographs with those measured during two experiments in which ~10 m^3 of sand and gravel (with 1–2% silt and clay by dry weight) was placed as a triangular wedge against a vertical gate 2 m high, saturated with water, and then suddenly released. Although the details of flow behavior varied between these two experiments, overall patterns of flow speed and depth were quite consistent. The match between data and model predictions of flow speeds and depths is reasonably good in most locations and reflects the overall unsteady, nonuniform behavior of the surging flows. The most significant predictive errors occur for cross sections 2 m downslope from the gate. These errors are not surprising, because considerable acceleration normal to the bed develops as the flow thins rapidly just downslope from the gate. Our depth-averaged model does not account for reaction forces exerted by the static bed in response to this slope-normal acceleration, and it consequently predicts too much thinning just downslope from the gate.

Model predictions of flow behavior farther downslope are more accurate. When debris flows reach cross sections 33 m and 67 m from the gate, their primary waveforms have markedly accelerated, elongated, and attenuated. Flow front depths stabilize when they attain values ~0.1 m, because unliquefied accumulations of coarse clasts at flow fronts provide resistance that impedes further thinning. Model predictions match the

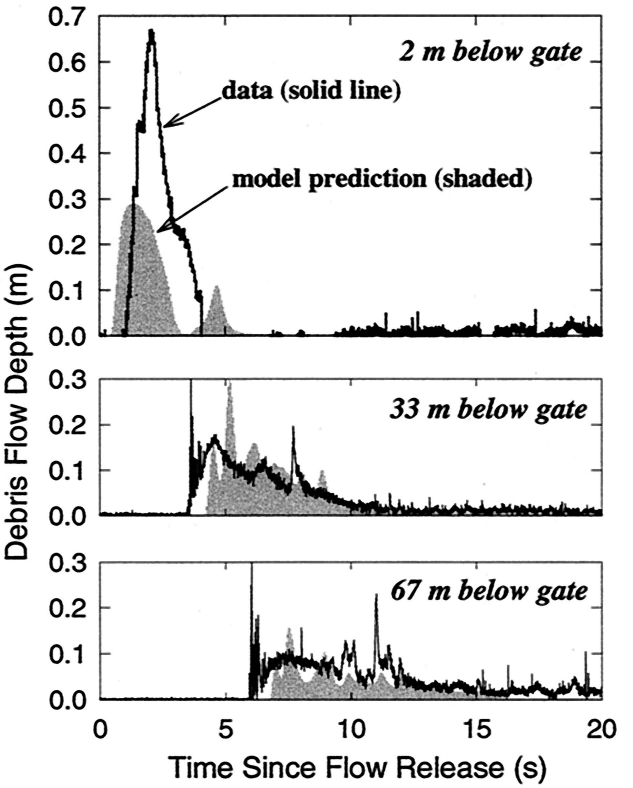

Figure 8. Comparison of measurements and model predictions of flow depths at three cross sections in a water-saturated debris flow at the USGS flume, July 24, 1995. Downslope distance is measured from the base of the gate at the flume head, and time is measured from the instant the gate opens.

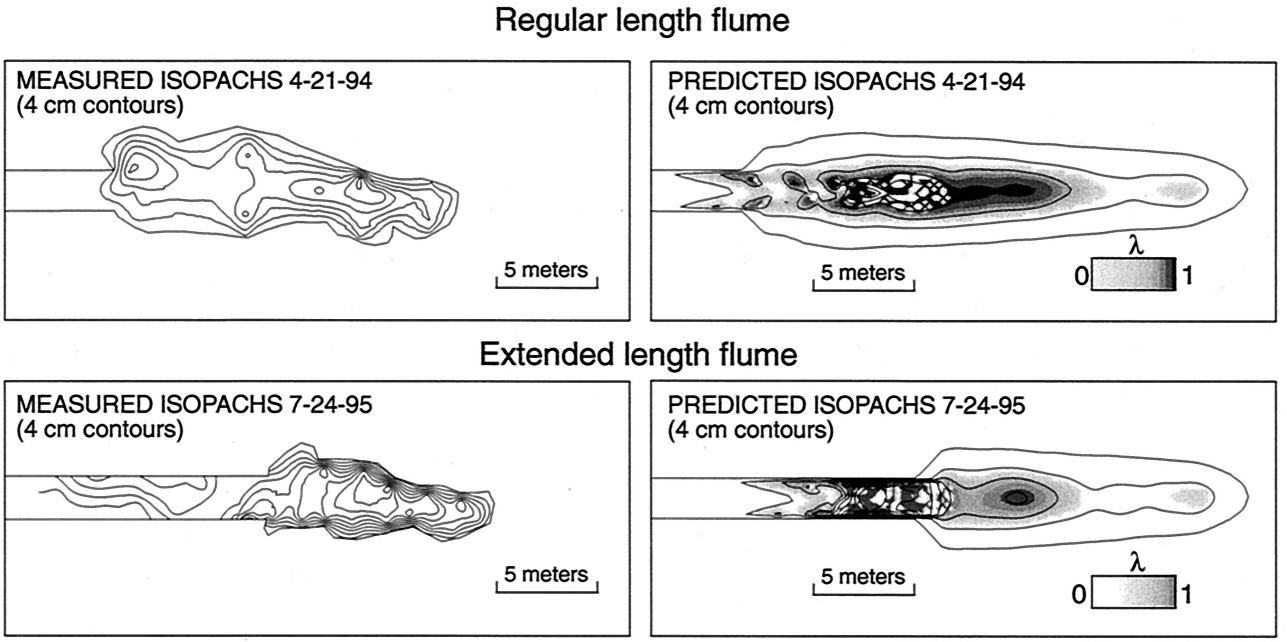

Figure 9. Isopach maps comparing measurements and model predictions of deposit locations and geometries produced by debris flows in the USGS flume. In one experiment the flume was in its regular configuration. In the other experiment the flume length was extended with concrete panels. Contours depict 4-cm isopachs of sediment thickness measured normal to the bed. Model results include predicted pore pressure distributions (indicated by values of λ) at the time of deposition. In each experiment, deposition concluded 17–18 s after flow release.

overall pattern of flow acceleration, elongation, and attenuation, although differences in some details are apparent.

Figures 7 and 8 reveal that short-period ($\sim$1 s) depth oscillations superposed on the primary waveforms are an obvious feature of both experimental data and model predictions. These oscillations reflect the presence of secondary surges that appear to develop spontaneously as roll wave instabilities [*Schonfeld*, 1996]. The secondary surges grow and sometimes coalesce, and they develop coarse-grained margins similar to but less conspicuous than that of the flow front. Model simulations of these secondary surges are rather simplistic. The simulated surges result from growth of infinitesimal depth perturbations that allow one or more of the kinematic criteria (24) to be satisfied locally. Where such a criterion is satisfied, the hydraulic diffusivity increases and pore pressures decay rapidly. Accompanying increases in Coulomb friction produce feedback that causes the perturbation to grow into a finite waveform. Such perturbations do not grow indefinitely, however, because they are stabilized by lateral stress transfer.

Model predictions of pore pressure distributions in the moving debris flows agree qualitatively with measurements reported by *Iverson* [1997a, 1997b] and *Major and Iverson* [1999]. The model correctly predicts pore pressure patterns characterized by low pressure (low λ) at the flow front and high pressure (high λ) in the liquefied debris that follows. This overall pore pressure pattern persists throughout the duration of debris flows, although it is affected by diffusion and advection and complicated by the secondary waves noted above.

Figure 9 compares model predictions and measurements of deposits formed by the two experimental debris flows characterized in Figures 7 and 8. In one experiment (April 21, 1994) the flow was allowed to spread laterally once it reached the runout surface 82.5 m downslope from the gate. In the other experiment (July 24, 1995) the flow was confined laterally by concrete panels that extended the flume side walls 7.4 m across the runout surface. Both deposits developed relatively planar upper surfaces and steep lateral and distal margins in the regions downstream from confined reaches. Lateral confinement caused the distal limit of the debris flow deposit to extend slightly further than in the unconfined case (Figure 9) and produced a somewhat larger maximum deposit thickness ($\sim$40 cm versus $\sim$25 cm) and considerably more deposition within the channelized reach. Examination and excavation of each deposit revealed that deposit interiors remained nearly liquefied immediately following deposition, while deposit perimeters were well-drained and had considerable frictional strength. This pattern matches that of many experimental data and field observations, which indicate that liquefied interiors and strong perimeters typify fresh debris flow deposits [*Major and Iverson*, 1999].

Figure 9 indicates that the computational results predict the mean runout, lateral spreading, thickness distributions, and pore pressure distributions of the experimental deposits quite well. Good predictions of lateral spreading and deposit thicknesses provide evidence that the DFE adequately represent multidimensional momentum transport. Good predictions of deposit centroids indicate that the DFE adequately represent overall energy dissipation in variably liquefied flows.

The most obvious misfit between the predictions and data shown in Figure 9 involves the distal limit of runout. Predictions produce deposits that extend too far and taper too gradually in the downstream direction. These tapering distal deposits result mostly from downstream numerical creep of the nearly static flow front, which occurs while trailing debris accumulates and comes to rest upstream. Numerical creep arises from imperfect balancing of source terms and flux terms, a

difficulty inherent in all Riemann methods. This difficulty is most apparent when flux terms diminish (as in formation of static deposits), but it might be overcome by static source term balancing schemes similar to that devised recently by *LeVeque* [1998]. We have not yet devised such a scheme for the DFE.

Predicted pore pressure distributions (depicted in Figure 9 by shading that represent λ) in general match those inferred from data and observations [*Major and Iverson*, 1999]. Zones of low pore pressure interspersed in high-pressure regions denote the static remains of secondary wave fronts that advected low pore pressures into the deposit. As a result, the thickest parts of deposits coincide with the static remains of secondary waves.

Predicted deposits shown in Figure 9 have lateral margins that are more tapered and less abrupt than those of deposits measured in experiments. This discrepancy results in part from the same numerical creep that affects our predictions of distal deposit limits and affects our predictions of static regions in dry granular flows. Numerical creep of deposits is most severe in partially liquefied flows, however. Such flows decelerate and form deposits gradually (in contrast to abruptly decelerating dry granular flows), and numerical creep is exacerbated where deposits remain nearly static for the longest time.

5. Discussion

The overall success of our predictive model leads us to draw upon Coulomb mixture theory to interpret phenomena observed in our experiments and in the field. The theory explains several key aspects of debris flow and granular avalanche behavior that have not been explained previously.

Flow front propagation is a crucial aspect of any rapid, gravity-driven mass movement. Comparison of our experimental and computational results for dry grain flow through a wide gate (Figure 5) provides the clearest test of flow front speed predictions because the flow is nearly one-dimensional and has few complications due to multidimensional momentum transport and no complications due to pore fluid pressure. In a fully one-dimensional flow the theoretical speed of a flow front moving to the right, for example, is given by the Riemann invariant of the left-going wave emanating from the front, $I_L = \bar{v}_x|_L + 2c_L$ (equation (21)). This theoretical result predicts the flow front motion observed in the center of our miniature flume almost exactly. Good correspondence between theoretical predictions and experimental data provide evidence that the expression for c derived from Coulomb mixture theory (equation (12)) is correct. The correspondence implies that c does, indeed, govern information propagation in granular avalanches with lengths much greater than their depths.

The expression for c contains the lateral stress coefficient $k_{a/p}$, which is itself derived from the assumption that Coulomb masses simultaneously deform internally and slide along a rough bed [*Iverson*, 1997a]. Existence of distinct $k_{a/p}$ values for diverging and converging flows causes Coulomb masses to behave quite differently from liquids. For example, large values of $k_{a/p}$ apply in regions of flow convergence and produce large lateral stresses that can support steep surface gradients. On the other hand, $k_{a/p}$ values are low in areas of flow divergence, which occur where flows accelerate down steep slopes. Where flows are liquefied by high pore pressure, lateral stresses have hydrostatic values sustainable by liquids. Thus, if the perimeter of a flow or deposit acts as a Coulomb mass that encloses a liquefied flow interior, it forms a steep, resistive margin pushed from behind by liquefied debris that can support little or no shear stress (Figures 7–9). The interaction of resistive, high-friction margins and weak, more-fluid interiors typifies a number of geophysical flows, including debris flows, pyroclastic flows, and aa lava flows.

Multidimensional momentum transport is another key facet of most gravity-driven mass movements. Multidimensional momentum transport has the clearest effects in our experimental and computational results for dry grain flow through a narrow gate (Figure 6). Divergence and convergence that occur as grains pass through the gate greatly reduce average flow speed (relative to the wide-gate case without divergence and convergence) and produce strong Coulomb shear stresses on planes normal to the basal boundary. These transverse shear stresses (denoted in the governing equations by terms that include $\sin \varphi_{int}$) generate much of the resistance that impedes flow through the gate and causes some sediment to be stranded behind the gate. We infer that flow models without transverse shear stresses will not accurately simulate flow interactions with complex topography.

The same transverse shear stresses cause increased energy dissipation where deposits spread laterally. Consequently, the dry grain flow through the narrow gate dissipated energy more quickly and deposited more sediment above the break in slope (at 100 cm in Figures 5 and 6) than did the flow through the wide gate. Nonetheless, the differences in deposit geometries in these two cases are rather subtle. The deposits preserved little information about the rather different flows that formed them.

Deceleration and deposition of both dry grain flows and wet debris flows respond strongly to changes in bed slope. The response includes two components. One component reflects a simple trade-off between reduced driving stress and increased resisting stress that occurs as bed slopes decline. The other component depends on the magnitude of the centripetal acceleration term involving the local radius of bed curvature. In the x momentum equation, for example, the effect of bed curvature on the basal friction force is proportional to $\bar{v}_x^2/r_x$, whereas the effect of bed slope on the basal friction force is proportional to g_z [*Iverson and Denlinger*, this issue]. In gently sloping regions where flows decelerate and stop, $g_z \sim 10$ m/s^2 is typical, but $\bar{v}_x^2/r_x$ varies depending on flow speed and bed curvature. In our small-scale experiments, $\bar{v}_x^2/r_x g_z \sim 0.4$ was typical of flow deceleration, indicating that frictional braking in response to bed curvature was less important than braking due to the change in bed slope. In contrast, values $\bar{v}_x^2/r_x g_z \sim 2$ typified deceleration in our large-scale debris flow experiments, indicating that bed curvature locally dominated frictional braking. Clearly, effects of bed curvature must be incorporated in efforts to model geophysical flows, which may be very rapid and may encounter terrain with significant local curvature (small r_x).

Although the DFE simulate the effects of three-dimensional flow boundaries quite well, we have not yet applied our model to irregular terrain typical of natural landscapes. Testing of model predictions against data from natural flows is difficult because for uncontrolled natural flows it is difficult to separate the influences of the governing equations, parameter values, and initial and boundary conditions. Indeed, we believe that no satisfactory field tests of models of geophysical grain flows have ever been conducted. On the other hand, our model can be tested with additional controlled experiments and used to replicate field data. In this paper we emphasize the initial phase of testing, and field applications remain as a future endeavor.

Computation of pore pressure distributions in geophysical grain flows poses another future challenge. Because high pore pressures can reduce Coulomb friction very substantially, and because Coulomb friction causes most energy dissipation, erroneous pore-pressure distributions might cause large predictive errors. Errors are likely to be most significant where the balance of forces is most delicate, where flows commence and where they decelerate and form deposits. Our predictions of deposit locations and geometries for flume experiments with water-saturated sand and gravel benefitted from relatively tight constraints on initial conditions and key material properties such as the pore pressure diffusivity. Where constraints are weaker, accurate prediction will be more difficult. In our opinion, improved means of estimating pore pressure distributions hold the key to improved predictive modeling of geophysical flows.

6. Conclusions

Correspondence between model predictions and experimental data for diverse, variably fluidized grain flows provides evidence that the debris flow equations (DFE) adequately describe the flow physics and that the Riemann method adequately solves the DFE. Our tests of the DFE and Riemann solver involved no calibration of parameter values or tailoring of initial and boundary conditions. Similarly stringent tests are difficult if not impossible to achieve when model results are fitted to field data.

Analysis of the DFE leads to identification of a gravity wave speed c that differs from the speed of conventional shallow-water gravity waves. The new expression for c reveals a key distinction between models that assume grain-fluid flows act as liquids with modified viscosities [e.g., *Sousa and Voight*, 1991] and models such as the DFE that account for frictional grain interactions: intergranular Coulomb friction causes flow divergence or convergence and variable fluidization (liquefaction) to affect information propagation markedly. This information propagation governs important phenomena such as the speed of advancing flow fronts.

Numerical and experimental results indicate that three-dimensional flow paths can cause strong Coulomb shear stresses to develop on planes normal to the basal flow boundary. These stresses dissipate energy as flow encounters obstructions, and they may cause debris to lodge upslope of obstacles or in tight constrictions. Models that lack multidimensional momentum transport or Coulomb friction cannot represent this energy dissipation and lodging.

Effects of three-dimensional flow paths on patterns of deposition might be used to constrain interpretations of geophysical events for which no real-time data are available. However, our initial investigations of dry grain flows indicate that rather similar depositional patterns can result from differing initial conditions, flow durations, and flow geometries (Figures 5 and 6). We infer that depositional patterns might provide only weak constraints on flow behavior in some circumstances.

Flows that are partly fluidized or liquefied by intergranular fluid pressure move more efficiently than flows without fluid pressure. This increased efficiency cannot be interpreted as the result of a distinct, steady state rheology that governs momentum transport and energy dissipation. Instead, the apparent rheology evolves as pore fluid pressures evolve from a uniform state to a state typified by a pressurized flow interior and depressurized flow perimeter. This evolution is an intrinsic aspect of many geophysical flows, which are invariably unsteady and nonuniform. For water-saturated debris flows we simulate this evolution by assuming that pore fluid pressures initially rise to high levels and then simultaneously advect with the flow and diffuse normal to the flow boundary. Pore pressure advection and diffusion are influenced by development of coarse-grained flow fronts with increased diffusivities and consequent increased friction. Enhanced marginal friction produces flows with steep surge fronts that are absent in granular flows with homogeneous frictional resistance [e.g., *Savage and Hutter*, 1989, 1991]. Inhomogeneous friction also produces deposits with steep margins and relatively flat, fluid interiors that develop significant strength only during post-depositional sediment consolidation [cf. *Major and Iverson*, 1999].

Despite significant differences in material properties, similar geometries develop in diverse geophysical flows (debris avalanches, pyroclastic flows, aa lava flows, wet snow avalanches) in which a high-friction outer rind appears to impede the motion of a more-fluid, low-friction interior. Our model provides a mathematical and computational structure that can be applied with only minor modifications to these diverse flows. Consequently, we believe it is possible to simulate the behavior of a variety of geophysical flows without invoking rheological parameters or fitting coefficients that have questionable physical significance.

Acknowledgments. Matthew Logan performed the dry sand flow experiments described herein. Richard LaHusen, Jon Major, and several assistants helped conduct the large-scale debris flow experiments. Without the expert assistance of these individuals, our model tests would be much poorer. We thank Joseph Walder, Jeff Johnson, Jeremiah Brackbill, and two anonymous reviewers for thoughtful critiques of the manuscript. Any use of trade, product, or firm names is for descriptive purposes only and does not imply endorsement by the U.S. Government.

References

Alcrudo, F., and P. Garcia-Navarro, A high-resolution Godunov-type scheme in finite volumes for the 2-D shallow water equations, *Int. J. Numer. Methods Fluids*, *16*, 489–505, 1993.

Denlinger, R. P., R. A. Walters, D. Levish, and D. Ostenaa, Robust methods for flood routing over highly irregular terrain, paper presented at First Federal Interagency Hydrologic Modeling Conference, Sub comm. on Hydrol., U.S. Interagency Advis. Comm. on Water Data, Las Vegas, Nev., April 19–23, 1998.

Freeze, R. A., and J. A. Cherry, *Groundwater*, 604 pp., Prentice-Hall, New York, 1979.

Greve, R., T. Koch, and K. Hutter, Unconfined flow of granular avalanches along a partly curved surface, I, Theory, *Proc. R. Soc. London*, *Ser. A*, *445*, 399–413, 1994.

Harten, A., P. D. Lax, and B. Van Leer, On upstream differencing and Godunov-type schemes for hyperbolic conservation laws, *SIAM Rev.*, *25*(1), 35–61, 1983.

Hungr, O., A model for the runout analysis of rapid flow slides, debris flows, and avalanches, *Can. Geotech. J.*, *32*, 610–623, 1995.

Iverson, R. M., The physics of debris flows, *Rev. Geophys.*, *35*, 245–296, 1997a.

Iverson, R. M., Hydraulic modeling of unsteady debris-flow surges with solid-fluid interactions, in *Debris Flow Hazards Mitigation: Mechanics Prediction and Assessment*, edited by C. L. Chen, pp. 550–560, Am. Soc. of Civ. Eng., Reston, Va., 1997b.

Iverson, R. M., and R. P. Denlinger, Flow of variably fluidized granular masses across three-dimensional terrain, 1, Coulomb mixture theory, *J. Geophys. Res.*, this issue.

Iverson, R. M., and R. G. LaHusen, Friction in debris flows: Inferences from large-scale flume experiments, in *Hydraulic Engineering '93: Proceedings of the 1993 Conference of the Hydraulics Division of the American Society of Civil Engineers*, vol. 2, pp. 1604–1609, Hydraul. Div., Am. Soc. of Civ. Eng., Reston, Va., 1993.

Iverson, R. M., J. E. Costa, and R. G. LaHusen, Debris-flow flume at H. J. Andrews Experimental Forest, Oregon, *U.S. Geol. Surv. Open File Rep*., *92-483*, 2 pp., 1992.

Iverson, R. M., M. E. Reid, and R. G. LaHusen, Debris-flow mobilization from landslides, *Ann. Rev. Earth Planet. Sci*., *25*, 85–138, 1997.

LeVeque, R. J., Balancing source terms and flux gradients in high-resolution Godunov methods: The quasi-steady wave-propagation algorithm, *J. Comput. Phys*., *146*, 346–365, 1998.

Major, J. J., and R. M. Iverson, Debris flow deposition: Effects of pore fluid pressure and friction concentrated at flow margins, *Geol. Soc. Am. Bull*., *111*, 1424–1434, 1999.

Major, J. J., R. M. Iverson, D. F. McTigue, S. Macias, and B. K. Fiedorowicz, Geotechnical properties of debris-flow sediments and slurries, in *Debris Flow Hazards Mitigation: Mechanics Prediction and Assessment*, edited by C. L. Chen, pp. 249–259, Am. Soc. of Civ. Eng., Reston, Va., 1997.

Reid, M. E., R. G. LaHusen, and R. M. Iverson, Debris-flow initiation experiments using diverse hydrologic triggers, in *Debris Flow Hazards Mitigation: Mechanics Prediction and Assessment*, edited by C. L. Chen, pp. 1–11, Am. Soc. of Civ. Eng., Reston, Va., 1997.

Savage, S. B., and K. Hutter, The motion of a finite mass of granular material down a rough incline, *J. Fluid Mech*., *199*, 177–215, 1989.

Savage, S. B., and K. Hutter, The dynamics of avalanches of granular materials from initiation to runout, part I, Analysis, *Acta Mech*., *86*, 201–223, 1991.

Schonfeld, B., Roll waves in granular flows and debris flows, M.S. thesis, 160 pp., Dep. of Civ. Eng. and Appl. Mech., McGill Univ., Montreal, Que., Canada, 1996.

Sousa, J., and B. Voight, Continuum simulation of flow failures, *Geotechnique*, *41*, 515–538, 1991.

Toro, E. F., *Riemann Solvers and Numerical Methods for Fluid Dynamics*, 492 pp., Springer-Verlag, New York, 1997.

Vreugdenhil, C. B., *Numerical Methods for Shallow-water Flow*, 261 pp., Kluwer Acad., Norwell, Mass., 1994.

Wieland, M., Gray, J. M. N. T., and K. Hutter, Channelized free-surface flow of cohesionless granular avalanches in a chute with shallow lateral curvature, *J. Fluid Mech*., *392*, 73–100, 1999.

R. P. Denlinger and R. M. Iverson, U.S. Geological Survey, 5400 MacArthur Blvd., Vancouver, WA 98661. (roger@usgs.gov; riverson@usgs.gov)

(Received January 18, 2000; revised August 11, 2000;
accepted August 23, 2000.)